nature physics

Article

https://doi.org/10.1038/s41567-026-03504-z

Thermodynamic demonstration of tetracriticality and multicomponent superconductivity in UTe_2

Received: 2 April 2026

Accepted: 22 September 2026

Published online: 30 October 2026

Check for updates

Sahas Kamat[1], Jared Dans[2], Shanta Saha[2], Artem D. Kokovin[3], Johnpierre Paglione[2,4], Jörg Schmalian[3,5] & B. J. Ramshaw[1,4]

The candidate topological superconductor UTe_2 exhibits a complex phase diagram with multiple superconducting states, and the nature of their coexistence is not yet resolved. In particular, the apparent observation of two intersecting second-order phase boundaries at a triple point in the pressure–temperature phase diagram is thermodynamically forbidden. This suggests either a hidden phase transition or a fundamental misunderstanding of the superconductivity in this material. Here we observe an additional phase boundary that is characterized by an upward jump in the sound velocity. This is direct thermodynamic evidence for a phase transition in which superconducting order is lost on cooling. Our results establish a tetracritical point beyond which the ambient and pressure-induced superconducting order parameters form a multicomponent state. We use the measured phase diagram to demonstrate that strong competition between the two superconducting order parameters drives the loss of order when cooling, and leads to phase locking that suppresses superconducting fluctuations. These findings provide the definitive magnetic field–pressure–temperature phase diagram of UTe_2 and establish a thermodynamic foundation for multicomponent superconductivity.

Multicomponent superconductivity occurs when two (or more) order parameters condense: the most famous example—once thought to be the superconducting state of Sr_2RuO_4 (ref. 1)—is the chiral $p_x + ip_y$ state in ^{3}He (ref. 2). Multicomponent order parameters are a frequent ingredient for chiral topological superconductivity[3,4], but, so far, there are very few—if any—confirmed examples outside of ^{3}He.

UTe_2 currently stands as the most viable candidate for spin-triplet multicomponent superconductivity. Although it is generally agreed that the zero-field ambient-pressure state (SC1) is a single component[5,6], there is clear evidence for a distinct superconducting state (SC2) that emerges under hydrostatic pressure[7–10]. Whether these phases coexist in some region of the pressure–temperature phase diagram and form a multicomponent state is currently unknown.

The central challenge is the presence of an enigmatic multicritical point at $(P^\star, T^\star)$ in the pressure–temperature phase diagram, where the SC2 critical-temperature line terminates on the SC1 line (Fig. 1, star). Specific heat[7] and magnetization[9] measurements clearly indicate that all transitions are of the second order and occur in the bulk. However, a triple point of second-order phase transitions (Fig. 1b), is thermodynamically forbidden[11], whereas the additional second-order line required for a tetracritical point (Fig. 1a) has remained elusive. Attempts to resolve this puzzle have led to speculations ranging from a hidden

[1]Laboratory of Atomic and Solid State Physics, Cornell University, Ithaca, NY, USA. [2]Maryland Quantum Materials Center, Department of Physics, University of Maryland, College Park, MD, USA. [3]Institute for Theory of Condensed Matter, Karlsruhe Institute of Technology, Karlsruhe, Germany. [4]Canadian Institute for Advanced Research, Toronto, Ontario, Canada. [5]Institute for Quantum Materials and Technologies, Karlsruhe Institute of Technology, Karlsruhe, Germany. e-mail: bradramshaw@cornell.edu

https://doi.org/10.1038/s41567-026-03504-z

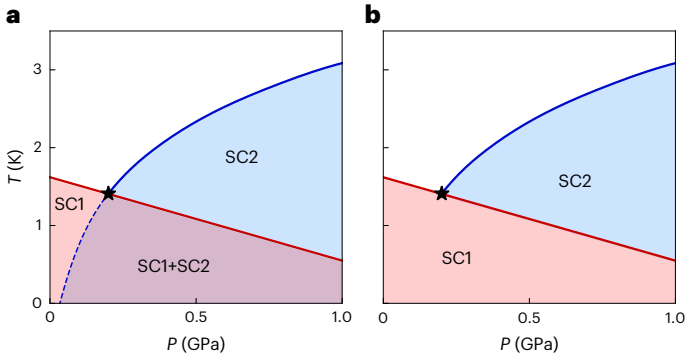


Fig. 1 | Proposed pressure–temperature phase diagrams for UTe_2. The elusive multicritical point is indicated by a black star. The well-established SC1 and SC2 phase boundaries are shown as solid red and blue lines, respectively. **a**, Proposed phase diagram in which the SC2 phase boundary extends past the critical point, with a region of coexistence of the SC1 and SC2 phases (shaded purple). Such a scenario implies the existence of a phase boundary indicated with a blue dashed line—this boundary has not yet been observed. **b**, Second proposal in which the SC2 phase boundary terminates on meeting the SC1 phase boundary. Given the weak heat capacity anomalies, this requires a third-order superconducting transition, where second derivatives of the free energy (such as heat capacity) remain continuous[7,11].

phase boundary[7–10] to a fine-tuned superconducting transition with a vanishing specific heat jump[7,10], suggesting the possibility of a third-order phase transition at $P\star$ (ref. 9).

Resolving these issues has implications that go beyond simply determining the topology of the UTe_2 phase diagram: for example, the continuation of the SC2 phase boundary past the critical point (Fig. 1a) implies a region in which the order parameters of SC1 and SC2 are simultaneously finite and with the potential for chiral topological superconductivity.

In this work, we use pulse-echo ultrasound to map the magnetic field–pressure–temperature (B–P–T) phase diagram of UTe_2 in the vicinity of the critical pressure $P\star$, where the two transitions meet. We find that the SC2 phase boundary extends past the SC1 phase boundary, leading to a region of two-component order SC1+SC2 in the phase diagram. We demonstrate that SC1 and SC2 interact strongly in this regime, with their competition leading to a loss of SC2 order on cooling. We construct a phenomenological Ginzburg–Landau (GL) theory that accurately reproduces the observed phase diagram, and draw inferences from the constraints that our data place on the GL parameters and, hence, on the microscopic theory of superconductivity in UTe_2.

Finally, we explore the magnetic field dependence of this phase diagram and construct a coherent picture of the field-induced and pressure-induced superconducting states. We show that the multicomponent phase is stabilized by a magnetic field and is accessible even at ambient pressure. Symmetry analysis of our c_{55} shear modulus data allows us to rule out the $A_u + B_{2u}$ and $B_{1u} + B_{3u}$ order parameter combinations, whether chiral or non-chiral, as candidates for the SC1+SC2 phase. Finally, the presence of a peak in the longitudinal sound attenuation at both T_{c1} and T_{c2} provides strong evidence that both SC1 and SC2 have sign-changing order parameters.

Experiment

Elastic moduli are thermodynamic coefficients: they are the second derivatives of a system's free energy with respect to strain. In this way, they are similar to specific heat—the second derivative of the free energy with respect to temperature. Like specific heat, we expect non-analyticity in the elastic moduli at a phase transition. Unlike specific heat in which there is only one coefficient, we expect different behaviours for the different elastic moduli depending on how they couple to the order parameter[12]. Generically, we expect jumps (discontinuities in elastic moduli) when the coupling is linear in strain and quadratic in order parameter and expect kinks (discontinuities in the temperature derivatives of the elastic moduli) when the coupling is quadratic in strain and quadratic in order parameter.

Previous ultrasound measurements on UTe_2 have demonstrated that the ambient and pressure-induced superconducting states couple strongly to the c_{11} and c_{33} (compressional) and c_{55} (shear) moduli[5,13]. We measure c_{11}, c_{33} and c_{55} as a function of temperature at fixed pressures between $P = 0$ and $P = 1$ GPa, focusing on pressures near the critical point at $P\star = 0.20$ GPa (Fig. 1). Full experimental details are given in ref. 13 and in Methods.

Results

Elastic moduli in zero magnetic field

Measurements of the c_{11} compressional elastic modulus at different pressures and in zero magnetic field are shown in Fig. 2b. At the lowest pressure—0.13 GPa—the transition to the SC1 state appears as a downward jump at T_{c1}. At pressures greater than $P\star$, two jumps appear at two transitions whose separation in temperature increases with increasing pressure. We identify the upper and lower transitions as T_{c2} and T_{c1}, respectively, based on previous measurements of the phase diagram[7,10,13]. From $P = 0.20$–0.22 GPa—pressures slightly greater than $P\star$—we measure an additional feature in c_{33}: an upward jump in c_{11}. The temperature at which this upward jump occurs does not correspond to either T_{c1} or T_{c2}, and we refer to it as T^*_{c2}.

We use the thermodynamic signatures in the elastic moduli at T_{c1} and T_{c2} to construct the phase diagram shown in Fig. 2a. These phase boundaries are consistent with previous work[7–10,13]. For reasons we will justify in the remainder of this manuscript, we place the T^*_{c2} points on a phase boundary connected to T_{c2} at the critical pressure $P\star$. This T^*_{c2} phase boundary has not been reported previously, and is the primary discovery of this work.

Loss of SC2 on cooling

The phase diagram shown in Fig. 2a suggests an unusual phenomenon: from $P = 0.20$ to 0.22 GPa, when decreasing the temperature from above the upper transition, UTe_2 first enters the SC2 phase at T_{c2}, then enters a mixed SC1+SC2 phase at T_{c1} and subsequently loses the SC2 component of the order parameter cooling through T^*_{c2}. Although the kinks and jumps in the elastic moduli identify the locations of these phase boundaries, we have not yet justified the assignment of T^*_{c2} to a phase boundary that connects to T_{c2}, nor have we justified the label SC1+SC2.

Second-order phase transitions are defined by discontinuities in certain derivatives of free energy[14]. The most familiar example is the specific heat, $C/T = -\partial^2 F/\partial T^2$. Typically, this jump must be upwards on cooling through T_c as the system enters the ordered state. In a superconductor, opening a gap restricts the electronic degrees of freedom[15], causing the entropy decrease more rapidly below T_c than in the normal state and producing the characteristic upward jump. For a phase boundary like T^*_{c2}, however, the heat capacity must jump downwards—behaviour that is generally required at a back-bent phase transition line (Methods). This has immediate implications for the elastic moduli.

Like the specific heat, elastic moduli are the second derivatives of free energy: $c_{ijkl} = \partial^2 F/\partial\varepsilon_{ij}\partial\varepsilon_{kl}$. For compression strains (such as ϵ_{xx}), the jumps in compression elastic moduli are related to the jump in the specific heat through an Ehrenfest relation. For $c_{11} \equiv c_{xxxx}$, the relationship is

$$\Delta c_{11} = -\frac{\Delta C}{T_c}\left(\frac{\partial T_c}{\partial \varepsilon_{xx}}\right)^2. \quad (1)$$

The coefficient $(\partial T_c/\partial\epsilon_{xx})$—the slope of T_c as a function of strain—always enters as the square, which means that Δc_{11} always has the opposite sign of ΔC. Conventionally, this means that the jump in a compression modulus at T_c must be downwards—a fact that is demonstrated at T_{c1}

https://doi.org/10.1038/s41567-026-03504-z

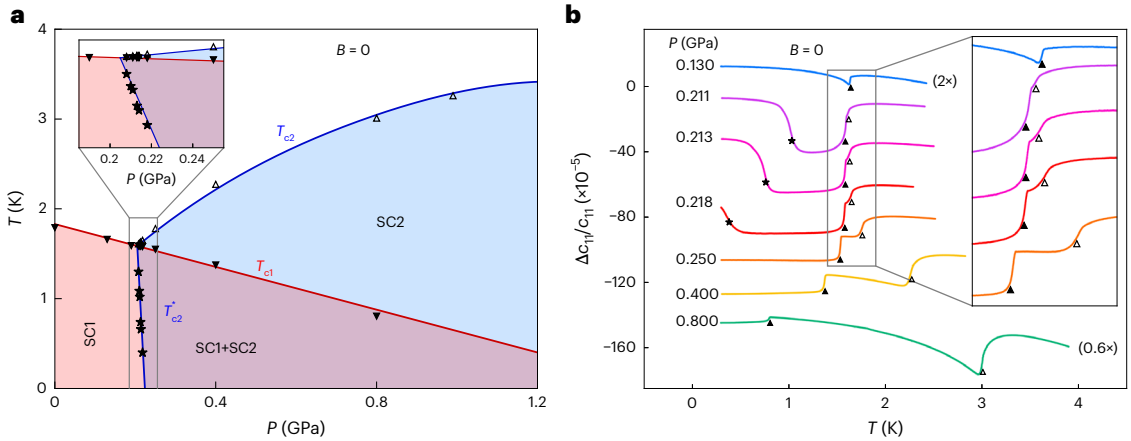


Fig. 2 | Phase diagram of UTe_2 near the tetracritical point. a, Zero-field phase diagram of UTe_2 constructed in this work. T_{c1}, T_{c2} and T^*_{c2} are represented by solid triangles, hollow triangles and stars, respectively. The solid red and blue lines are guides to the eye that represent the SC1 and SC2 phase boundaries, respectively. Regions in phase space in which the SC1 and SC2 order parameters are non-zero are shaded red and blue, respectively. Inset: phase diagram zoomed in around the tetracritical point, illustrating the back bending of the T^*_{c2} phase boundary. **b**, Select c_{11} elastic modulus data (full datasets are provided in Extended Data Figs. 1–9). For $P < 0.20$ GPa, we find a downward jump at T_{c1} when UTe_2 enters the SC1 state. Two distinct jumps at at T_{c1} and T_{c2} are visible for $P > 0.20$ GPa. Between $P = 0.20$ and 0.22 GPa, we find an upward jump at T^*_{c2} as the sample exits the SC2 superconducting state on cooling. Inset: zoomed-in c_{11} data showing two distinct jumps at T_{c1} and T_{c2} for pressures near $P\star$.

and T_{c2} in Fig. 2c, and which has been documented for many other phase transitions[16].

At $P = 0.213$ GPa, c_{11} first jumps downwards on cooling through $T_{c2} = 1.63$ K, and again at $T_{c1} = 1.58$ K. Then, at $T^*_{c2} = 1.0$ K, c_{11} jumps upwards. According to equation (1), the specific heat should jump downwards, as required for a system that has lost order on cooling. This is our primary evidence that T^*_{c2} marks the transition at which the SC2 order parameter is lost on cooling. We observe no hysteresis at T^*_{c2} when warming and cooling through the transition, demonstrating that this transition is of the second order (Methods describes that such a transition is fully consistent with thermodynamic constraints).

Having demonstrated that T^*_{c2} corresponds to a second-order phase transition in which order is lost on cooling, we assign it to the second branch of the SC1 phase boundary. This boundary is nearly vertical in the P–T phase diagram (Fig. 2a). This assignment is consistent with the fact that the jump upwards at T^*_{c2} returns the elastic modulus to a value very close to what it would have been had it gone through T_{c1} alone, as can be determined from the 0.13-GPa data.

Elastic moduli in a magnetic field

To explore the evolution of the T^*_{c2} phase boundary, we measure the c_{33} and c_{55} elastic moduli as a function of the magnetic field along the b axis and track T^*_{c2} across the full B_b–P–T phase diagram.

We construct field–temperature phase diagrams at four distinct pressures in the vicinity of $P\star$ (Fig. 3a–d). Below each phase diagram, we show the selected elastic moduli versus temperature curves that are used to construct these phase diagrams—full datasets are provided in Extended Data Figs. 1–9. Figure 3e–h shows select c_{55} curves, and Fig. 3i–l shows select c_{33} curves.

We use kinks in c_{55} and jumps in c_{33} to identify the phase boundaries: T_{c1} is indicated with solid triangles, and T_{c2} is indicated with hollow triangles. Note that c_{55} exhibits jumps only when the order parameters satisfy certain symmetry conditions[5]; the absence of a jump in c_{55} here rules out the $A_u + B_{2u}$ and $B_{1u} + B_{3u}$ combinations, both chiral and non-chiral, for the SC1+SC2 state (Methods). We find that the pressure-induced SC2 phase is indeed topologically connected to the field-induced phase for $B \| b$ (not the orphan SC3 phase at higher fields away from the b axis[17]), consistent with previous reports[10].

The central result contained in these data is the field and pressure evolution of T^*_{c2}. Similar to zero pressure (but broadened slightly because of the magnetic field), we find upward jumps in c_{33} on cooling through T^*_{c2}. These phase boundaries represent the transition from the mixed SC1+SC2 phase to the pure SC1 phase—to our best knowledge, these phase boundaries have never been reported.

The T^*_{c2} boundary in the field–temperature phase diagram evolves rapidly with pressure. At $P = 0.11$ GPa, the tetracritical point is located near 7 T and 1.25 K. As the pressure is increased, the field value at which this tetracritical point occurs decreases rapidly, reaching zero field at $P\star$ and providing the tetracritical point shown in Fig. 2. After $P\star$, the pure SC1 phase is pinched off at zero magnetic field, confined to a small pocket at low temperatures and finite magnetic fields.

Full B–P–T phase diagram

The phase diagrams we have constructed in the b-axis magnetic field, pressure and temperature can be combined into a three-dimensional B_b–P–T diagram, as shown in Fig. 4 (details of how this phase diagram is constructed are given in the caption). The two-component state SC1+SC2 occupies a large region of phase space, extending down to zero pressure for magnetic fields $18 > B_b > 12$ T. We show an ambient-pressure phase diagram as a function of B_b in Extended Data Fig. 4.

Analysis

Competing superconducting orders

The phase diagram shown in Fig. 4 is highly unusual in that the SC2 phase boundary bends back on itself when it hits the SC1 phase boundary. This leads to a narrow pressure range over which the SC2 order parameter is lost on cooling: between 0.20 and 0.22 GPa, decreasing T causes the system to first enter and then exit the SC2 state. Can such an exotic phase diagram be explained within a GL framework? Similar back bending was observed at the intersection of antiferromagnetism and superconductivity in iron pnictides[18,19]. There, it was explained in terms of a competition between the superconducting and antiferromagnetism order parameters[19]. In this section, we use the zero-field phase diagram to construct a phenomenological GL theory of two interacting superconducting order parameters.

We begin with two non-interacting order parameters, ψ_1 and ψ_2, corresponding to the SC1 and SC2 states. Each independent ψ_i has a free energy density $F_i = \frac{a_i}{2}|\psi_i|^2 + \frac{u_i}{4}|\psi_i|^4$. Without any interaction between them, the total free energy is simply $F = F_1 + F_2$, with a phase

https://doi.org/10.1038/s41567-026-03504-z

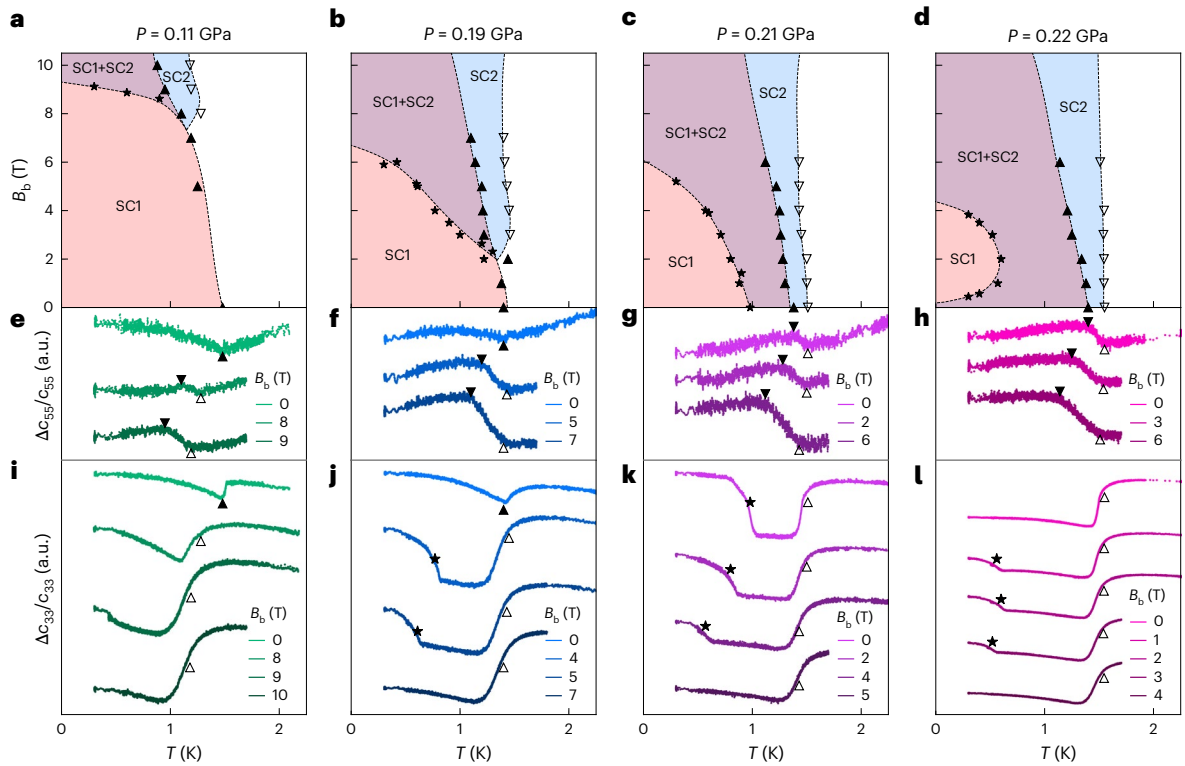


Fig. 3 | Field-temperature phase diagrams of UTe_2 at fixed pressure. The corresponding c_{55} and c_{33} data are shown directly below **a**–**d**. T_{c1}, T_{c2} and T^*_{c2} measured in this work are represented by solid triangles, hollow triangles and stars, respectively. **a**–**d**, Phase diagrams. Regions in phase space in which the SC1, SC2 and SC1+SC2 order parameters are non-zero are shaded in red, blue and purple, respectively. **e**–**h**, c_{55} elastic modulus data. T_{c1} and T_{c2} are seen as sharp kinks in the data. **i**–**l**, c_{33} elastic modulus data. The downward jumps on cooling correspond to T_{c1} or T_{c2}, whereas the upward jumps correspond to T^*_{c2}.

diagram in the form shown in Fig. 1a—two phase boundaries crossing one another without any change in slope.

However, the experimental SC2 phase boundary exhibits a substantial change in slope when it hits the SC1 phase boundary. To account for this, we add the lowest-order, symmetry-allowed terms that couple ψ_1 and ψ_2:

$$F = F_1 + F_2 + \frac{\gamma_1}{2}|\psi_1|^2|\psi_2|^2 + \frac{\gamma_2}{4}(\psi_1^2\psi_2^{*2} + \text{h.c.}) \qquad (2)$$

Here γ_1 couples the two order parameter magnitudes, whereas γ_2 locks the relative phase of the two complex order parameters. The sign of γ_2 determines whether the SC1+SC2 breaks time reversal ($\gamma_2 > 0$) or not ($\gamma_2 < 0$). The competition of the two phases is governed in either case by the parameter $\gamma \equiv \gamma_1 - |\gamma_2|$.

There are three key features of the experimental phase diagram that constrain the GL theory: (1) the phase lines meet at a tetracritical point, (2) the slope of T_{c1} versus pressure is almost unaffected by the intersection with T_{c2} and (3) the SC1↔SC1+SC2 phase boundary bends backwards. These three observations give rise to the following three constraints:

$$\begin{array}{ll} \text{Observation} & \text{Constraint} \\ \text{Tetracritical point} & 0 < \gamma < \sqrt{u_1 u_2} \\ T_{c1}\text{ unaffected} & \gamma \ll u_2 \\ \text{Back bending} & \gamma > u_1 \end{array}, \qquad (3)$$

where u_i are the quartic coefficients of the uncoupled theory and we use a convention for the quadratic coefficients a_i (Methods).

These constraints naturally explain the observed hierarchy of specific heat jumps at the various transitions. Specifically, they explain why the jump at the upper T_{c2} transition is small compared with the jump at T_{c1}—a fact that led to various alternative explanations of the phase diagram. First, the ratio of the specific heat jumps at the

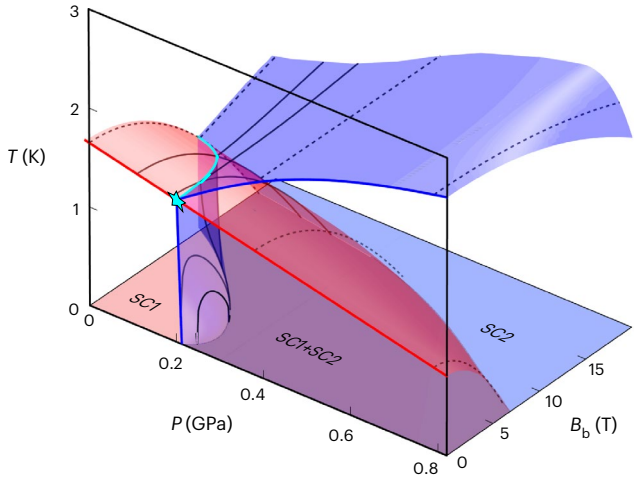


Fig. 4 | B–P–T phase diagram of UTe_2. The SC1 and SC2 phase boundaries are represented by red and blue sheets, respectively. The $B = 0$ plane is indicated by a black frame, on which solid red and blue lines represent the zero-field phase boundaries from this work (Fig. 2a). Solid black lines represent the constant-pressure phase boundaries shown in Fig. 3a–d. Dashed black lines are adapted from ref. 10. The zero-temperature ground states of the system are shown on the $T = 0$ plane. The tetracritical point in the P–T plane ($P^\star$, $T^\star$), indicated with a light-blue star) becomes a line of tetracritical points in B_b–P–T space, indicated by the light-blue line. This line terminates at 12 T and 1 K at ambient pressure. Between 12 and 18 T, the SC1+SC2 state exists at ambient pressure (Methods provides an ambient-pressure phase diagram).

https://doi.org/10.1038/s41567-026-03504-z

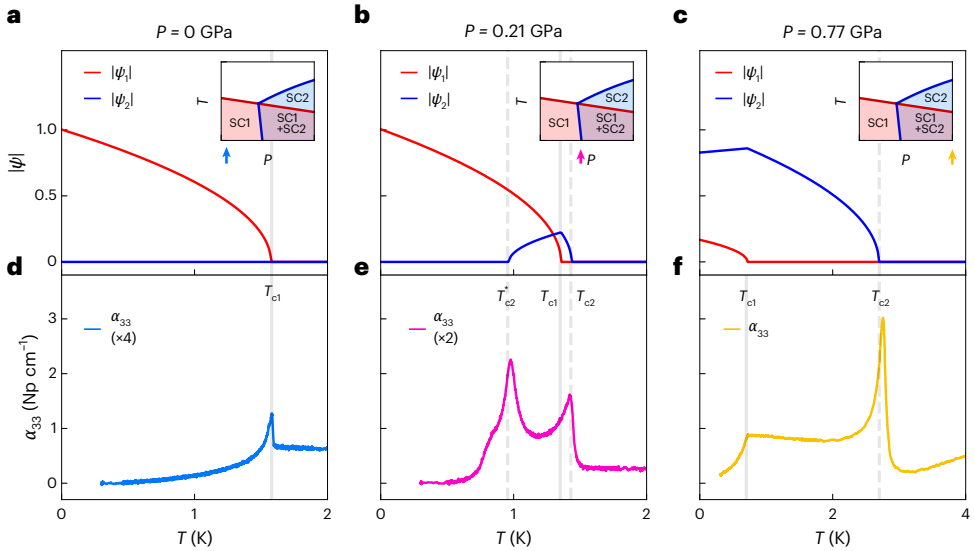


Fig. 5 | Order parameter competition in UTe_2. a–c, Order parameter magnitudes for SC1 ($|\psi_1|$) and SC2 ($|\psi_2|$) states versus temperature at different pressures. T_{c1} is indicated by a solid grey line, whereas T_{c2} and T^*_{c2} are indicated by dashed grey lines. Insets show where each pressure lies on the phase diagram of Fig. 2a. **d–f**, Ultrasonic attenuation α_{33} versus temperature at different pressures. We find an order parameter relaxation peak as the sample enters the SC1 state at 0 GPa, and as the sample enters and exits the SC2 state at 0.21 GPa. At 0.77 GPa, anomalously large phase fluctuations[13] cause the ultrasonic attenuation inside the SC2 state to be larger than the normal-state value. Below T_{c1}, α_{33} is suppressed by the growth of the SC1 order parameter that provides phase stiffness and suppresses fluctuations.

transitions from the normal metal to the single-component states is given by the inverse ratio of the quartic interactions, that is, $(\Delta C/T|_{T_{c1}})/(\Delta C/T|_{T_{c2}}) = u_2/u_1$. Equation (3) requires this ratio to be large—the jump at T_{c1} should be much larger than the jump at T_{c2}—which is fully consistent with the data of refs. 7,8,10. Second, the jump at the transition from SC2 to SC2+SC1 is given by $\Delta C/T|_{T_{c1}} = \Delta C/T|_{T_{c2}} \times \frac{(u_2-\gamma)^2}{u_1u_2-\gamma^2}$. The above conditions require that the jump at T_{c1} to the SC1+SC2 phase is much larger than the jump at T_{c2} to the SC2 phase, which is again in full agreement with the data[7,8,10]. Finally, a consequence of back bending is that the jump at T^*_{c2} is negative: $\Delta C/T|_{T^*_{c2}} = -\Delta C/T|_{T_{c1}} \times \frac{(u_1-\gamma)^2}{u_1u_2-\gamma^2}$, as discussed earlier. Full calculations are given in Methods.

With the GL parameters constrained by the phase diagram, the competition between SC1 and SC2 can be visualized by plotting $|\psi_1|$ and $|\psi_2|$ as a function of temperature alongside the α_{33} sound attenuation coefficient. Sound attenuation in a metal at low temperatures is dominated by the conduction electrons—in the superconducting state, the sound attenuation generally decreases as the normal quasiparticles are gapped out (further discussion is provided elsewhere[13]). Figure 5a illustrates this at ambient pressure: the sound attenuation decreases to zero as $|\psi_1|$ grows with decreasing temperature. Near T_{c1}, we find an order parameter fluctuation peak in α_{33}, which is indicative of a sign-changing gap; this is discussed in ref. 13 and seen in other heavy-fermion superconductors[20,21].

Competition between the two order parameters is clearly visible at $P = 0.21$ GPa—slightly greater than $P\star$ (Fig. 5b). The growth of $|\psi_2|$ below T_{c2} is sharply curtailed by the appearance of $|\psi_1|$ at T_{c1}. Below T_{c1}, ψ_1 grows unimpeded, whereas ψ_2 is suppressed. This suppression is complete by T^*_{c2}. The ultrasonic attenuation α_{33} (Fig. 5e) shows attenuation peaks at both entrance to and exit out of the SC2 phase, consistent with SC2 also having a sign-changing gap.

At the highest pressure, that is, $P = 0.77$ GPa, $|\psi_2|$ has a much broader region to establish itself before being truncated by the appearance of $|\psi_1|$ (Fig. 5c). Sound attenuation is the strongest here: below the fluctuation peak at T_{c2}, the sound attenuation remains larger than its normal-state value all the way down to T_{c1}, at which point it drops towards zero. We attribute this excess sound attenuation to the anomalously low phase stiffness of the SC2 phase[13]—an attribution also consistent with the constraints in equation (3) and with magnetic susceptibility measurements[9]. Within our GL analysis, we show that the quartic coupling term $e(\psi_1^2\psi_2^{*2} + \text{h.c.})$ locks the relative phase of the two order parameters, allowing the SC2 state to gain phase stiffness from the SC1 state, suppressing the phase fluctuations that produce the anomalous sound attenuation for $T_{c1} < T < T_{c2}$ (Methods).

Discussion

Our discovery of the phase transition line at T^*_{c2} establishes that (1) $(P\star, T\star) \approx (0.20\ \text{GPa}, 1.6\ \text{K})$ is a tetracritical point; (2) this extends to a tetracritical line in the B–P–T phase diagram; (3) the SC2 phase is strongly influenced by the SC1 phase, but not the other way around; and (4) there is a region in the B–P–T phase diagram with multicomponent superconductivity. The obvious question is whether this multicomponent state is time-reversal-symmetry (TRS) breaking and possibly topological.

Whether or not the SC1+SC2 state breaks time reversal depends on the sign of γ_2 in equation (2). A negative value implies a trivial combination of the two order parameters with the same phase, whereas a positive value implies that the relative phase between the two order parameters is π/2, leading to a chiral $\psi_1 + i\psi_2$ state that breaks TRS. As we discuss in Methods, if the spin structure of the two triplet states in momentum space is similar, we find that $\gamma_2 > 0$ and that TRS breaking is favoured in SC1+SC2.

An intriguing feature of the phase diagram is that the SC1+SC2 phase expands with an increasing magnetic field (Fig. 4). Several mechanisms could account for this behaviour. First, the field-induced expansion of the SC1+SC2 phase could arise from a TRS-breaking multicomponent superconducting state. Such a state possesses an intrinsic TRS-antisymmetric orbital moment[3] that couples linearly with a magnetic field, lowering the energy of the SC1+SC2 state. Second, it was recently proposed in ref. 22 that both SC2 and high-field re-entrant (SC3) superconducting phases are stabilized by an internal exchange field via the Jaccarino–Peter effect, which could similarly favour the SC1+SC2 phase at finite field without the need for TRS breaking by the ordered state itself. Finally, given the proximity of SC2 to

a metamagnetic phase transition[17,22,23], it is possible that the pairing interaction itself is strengthened by a magnetic field.

The hierarchy of the quartic couplings, $u_1 < \gamma \ll u_2$, has clear consequences for the electronic states that form the Cooper pairs. Such a pronounced separation of coupling strengths requires that the orbitals responsible for the large density of states—revealed by the residual specific heat and cyclotron mass—have a substantially larger weight in the pair wave function of SC1 than of SC2 (Methods). This insight imposes a stringent constraint on any microscopic theory of the pairing mechanism in UTe_2.

The accessibility of the multicomponent state at ambient pressure using a magnetic field motivates further study with probes directly sensitive to the excitations of a topological superconductor.

Online content

Any methods, additional references, Nature Portfolio reporting summaries, source data, extended data, supplementary information, acknowledgements, peer review information; details of author contributions and competing interests; and statements of data and code availability are available at https://doi.org/10.1038/s41567-026-03504-z.

References

1. Kallin, C. Chiral *p*-wave order in Sr_2RuO_4. *Rep. Prog. Phys.* **75**, 042501 (2012).
2. Vollhardt, D. & Wölfle, P. *The Superfluid Phases of Helium 3* (Courier Corporation, 2013).
3. Sigrist, M. & Ueda, K. Phenomenological theory of unconventional superconductivity. *Rev. Mod. Phys.* **63**, 239–311 (1991).
4. Sato, M. & Ando, Y. Topological superconductors: a review. *Rep. Prog. Phys.* **80**, 076501 (2017).
5. Theuss, F. et al. Single-component superconductivity in UTe_2 at ambient pressure. *Nat. Phys.* **20**, 1124–1130 (2024).
6. Rosa, P. F. S. et al. Single thermodynamic transition at 2 K in superconducting UTe_2 single crystals. *Commun. Mater.* **3**, 33 (2022).
7. Braithwaite, D. et al. Multiple superconducting phases in a nearly ferromagnetic system. *Commun. Phys.* **2**, 147 (2019).
8. Thomas, S. M. et al. Evidence for a pressure-induced antiferromagnetic quantum critical point in intermediate-valence UTe_2. *Sci. Adv.* **6**, eabc8709 (2020).
9. Wu, Z. et al. Magnetic signatures of pressure-induced multicomponent superconductivity in UTe_2. *Phys. Rev. Lett.* **134**, 236501 (2025).
10. Vasina, T. et al. Connecting high-field and high-pressure superconductivity in UTe_2. *Phys. Rev. Lett.* **134**, 096501 (2025).
11. Yip, S. K., Li, T. & Kumar, P. Thermodynamic considerations and the phase diagram of superconducting UPt_3. *Phys. Rev. B* **43**, 2742–2747 (1991).
12. Ghosh, S. et al. Thermodynamic evidence for a two-component superconducting order parameter in Sr_2RuO_4. *Nat. Phys.* **17**, 199–204 (2021).
13. Kamat, S. et al. Vanishing phase stiffness and fluctuation-dominated superconductivity: evidence for inter-band pairing in UTe_2. *Phys. Rev. X* **16**, 041006 (2026).
14. Callen, H. B. *Thermodynamics and an Introduction to Thermostatistics* (John Wiley & Sons, 1991).
15. Tinkham, M. *Introduction to Superconductivity* (Courier Corporation, 2004).
16. Rehwald, W. The study of structural phase transitions by means of ultrasonic experiments. *Adv. Phys.* **22**, 721–755 (1973).
17. Ran, S. et al. Extreme magnetic field-boosted superconductivity. *Nat. Phys.* **15**, 1250–1254 (2019).
18. Nandi, S. et al. Anomalous suppression of the orthorhombic lattice distortion in superconducting $Ba(Fe_{1-x}Co_x)_2As_2$ single crystals. *Phys. Rev. Lett.* **104**, 057006 (2010).
19. Fernandes, R. M. & Schmalian, J. Competing order and nature of the pairing state in the iron pnictides. *Phys. Rev. B* **82**, 014521 (2010).
20. Bishop, D. J. et al. Ultrasonic attenuation in UPt_3. *Phys. Rev. Lett.* **53**, 1009–1011 (1984).
21. Batlogg, B. et al. Ultrasound studies of the heavy fermion superconductors UPt3, UBe13 and (U, Th)Be13. *Physica B+C* **135**, 23–26 (1985).
22. Helm, T. et al. Field-induced compensation of magnetic exchange as the possible origin of reentrant superconductivity in UTe_2. *Nat. Commun.* **15**, 37 (2024).
23. Rosuel, A. et al. Field-induced tuning of the pairing state in a superconductor. *Phys. Rev. X* **13**, 011022 (2023).

Publisher's note Springer Nature remains neutral with regard to jurisdictional claims in published maps and institutional affiliations.

Springer Nature or its licensor (e.g. a society or other partner) holds exclusive rights to this article under a publishing agreement with the author(s) or other rightsholder(s); author self-archiving of the accepted manuscript version of this article is solely governed by the terms of such publishing agreement and applicable law.

© The Author(s), under exclusive licence to Springer Nature Limited 2026

Methods

Pressure determination

Samples were pressurized at room temperature in a piston anvil cell using a hydraulic press, with the resistance of a manganin coil mounted inside the pressure cell serving as a manometer. At cryogenic temperatures, pressure was determined by benchmarking the measured T_{c1} and T_{c2} values against existing literature[7,9,10]. We show the inferred pressures at low temperature (P_{4K}) versus the pressures measured by the manganin coil at room temperature (P_{300K}) in Extended Data Fig. 1a. We obtain a good fit to a second-order polynomial.

To obtain a high degree of control over the relative pressure of our sample close to the tetracritical point, we tune the pressure by carefully controlling the pressure cell volume. Measurements of the pressure as measured by the manganin coil versus the change in length of the pressure cell are shown in Extended Data Fig. 1b. We find that the data fit well to a fourth-order polynomial, with the observed curve reminiscent of a Boyle's law $P \propto 1/V$ dependence.

Using the cryogenic pressure dependence we measure in Extended Data Fig. 1a, we construct a function that relates the change in length of the cell (ΔL) to the low-temperature pressure (P_{4K}). Although the uncertainty in the fit in Extended Data Fig. 1a means our absolute pressure determination is only accurate up to 0.05 GPa, we can accurately determine the relative pressures around the tetracritical point. Knowing the slope of the pressure versus length curve (dP/dL) allows us to tune the (relative) pressure of the cell by controlling its volume.

As a consistency check, we also measure c_{33} from 4 to 100 K at different pressures (Extended Data Fig. 1d). The minimum in the data seen at temperatures near 15 K can be attributed to Kondo softening of the lattice. The magnitude of this dip is sensitive to changes in pressure, and the value of c_{33} at the minimum decreases with increasing pressure. We observe this to be true at even the smallest pressure increases we measure in this work, with larger pressure increases leading to larger changes in the Kondo softening, thereby providing a qualitative consistency check to our pressure measurement procedure.

To observe discontinuities in thermodynamic quantities such as the elastic modulus or specific heat at T^*_{c2}, the pressure inhomogeneity in a measurement has to be smaller than the pressure width of the phase boundary itself. Since the steep T^*_{c2} phase boundary is 0.01 GPa wide, any measurement of T^*_{c2} needs a smaller pressure inhomogenity. Our technique has an advantage in this regard because we measure a much smaller sample volume than other techniques such as specific heat (Extended Data Fig. 1e).

Phase stiffness of the SC1+SC2 state

In the 'Analysis' section, we attribute the decrease in attenuation in the SC1+SC2 state to an increase in the phase stiffness as the SC1 order parameter grows below T_{c1}. Here we sketch out a simple GL theory to show how the SC2 state acquires the phase stiffness of the SC1 state.

In the SC2 state alone, the system is described by a free energy density (F) of the form

$$F = F_n + \int \frac{d\mathbf{r}}{V}\left[\frac{a_2}{2}(T)|\psi_2|^2 + \frac{u_2}{4}|\psi_2|^4 + K_2|\nabla\psi_2|^2\right] \quad (4)$$

where F_n is the free energy density of the normal state, and a_2, u_2 and K_2 are GL parameters corresponding to the SC2 state. The last (gradient) term in this equation penalizes spatial variation in the order parameter $\psi_2 = |\psi_2|e^{i\theta_2(x)}$ via an increase in the free energy density. For a sinusoidal spatial variation in the phase of the order parameter of the form $\theta_2(x) = \theta_0 e^{ikx}$, the increase in free energy density is $\Delta F = K_2|\psi_2|^2\left(k^2\theta_0^2\right)$. The prefactor $\kappa = K_2|\psi_2|^2$ is known as the phase stiffness. This quantity is anomalously low for the SC2 state, leading to large spatial fluctuations in $\theta_2(x)$ that cause a larger than normal-state attenuation below T_{c2} (ref. 13).

When the sample enters the combined SC1+SC2 state, the total free energy density is given by

$$\begin{aligned} F_{tot} = F_n &+ \int \frac{d\mathbf{r}}{V}\left[\frac{a_2}{2}|\psi_2|^2 + \frac{u_2}{4}|\psi_2|^4 + K_2|\nabla\psi_2|^2\right] \\ &+ \int \frac{d\mathbf{r}}{V}\left[\frac{a_1}{2}|\psi_1|^2 + \frac{u_1}{4}|\psi_1|^4 + K_1|\nabla\psi_1|^2\right] \\ &+ \int \frac{d\mathbf{r}}{V}\left[\frac{\gamma_2}{4}\left(\psi_1^2\psi_2^{*2} + \psi_1^{*2}\psi_2^2\right) + \frac{\gamma_1}{2}\left(|\psi_1|^2|\psi_2|^2\right)\right] \end{aligned} \quad (5)$$

The term $\gamma_2(\psi_1^2\psi_2^{*2} + \psi_1^{*2}\psi_2^2)$ locks the relative phases of the two order parameters, such that if $\theta_2(x) = \theta_0 e^{ikx}$, θ_1 is forced to be

$$\theta_1(x) = \theta_0 e^{ikx} + \begin{cases} \pi/2 & \gamma_2 > 0 \\ 0 & \gamma_2 < 0 \end{cases} \quad (6)$$

Thus, SC2 phase fluctuations lead to an increased energy cost by inducing fluctuations in the SC1 state. The total increase in free energy density is given by

$$\Delta f = \left(K_1|\psi_1|^2 + K_2|\psi_2|^2\right) \times \left(k^2\theta_0^2\right) \quad (7)$$

The total phase stiffness of the SC1+SC2 state becomes $\kappa = K_1|\psi_1|^2 + K_2|\psi_2|^2$. The SC1 state is known to have a larger phase stiffness, and $K_1 \gg K_2$. As $|\psi_1|$ grows below T_{c1}, κ rapidly increases, suppressing phase fluctuations of the SC2 state and, thus, leading to decreased attenuation.

GL theory and constraints from the phase diagram

The GL expansion for a two-component superconductor with non-symmetry-related components, as it occurs for two distinct one-dimensional irreducible representations (irrep) is given as

$$\begin{aligned} F(\psi_1,\psi_2) = &\frac{a_1}{2}|\psi_1|^2 + \frac{u_1}{4}|\psi_1|^4 + \frac{a_2}{2}|\psi_2|^2 + \frac{u_2}{4}|\psi_2|^4 \\ &+ \frac{\gamma_1}{2}|\psi_1|^2|\psi_2|^2 + \frac{\gamma_2}{4}\left(\psi_1^*\psi_1^*\psi_2\psi_2 + \text{h.c.}\right) \end{aligned}, \quad (8)$$

where

$$a_j = a_{j,0}\left(T - T^{(0)}_{c,j}\right). \quad (9)$$

The $T^{(0)}_{c,j}$ are the transitions in which the individual order parameters emerge first. The last term in equation (8) determines the relative phase $\phi_1 - \phi_2$ of the two order parameters $\psi_j = A_j e^{i\phi_j}$. If $\gamma_2 > 0$, the relative phase is $\pm\pi/2$ and TRS is broken if both order parameters occur simultaneously. If γ_2 is negative, TRS is preserved. Let us fix the global phase to be zero. Then, it follows that

$$F(A_1,A_2) = \frac{a_1}{2}A_1^2 + \frac{u_1}{4}A_1^4 + \frac{a_2}{2}A_2^2 + \frac{u_2}{4}A_2^4 + \frac{\gamma}{2}A_1^2A_2^2, \quad (10)$$

where $\gamma = \gamma_1 - |\gamma_2|$. Let us further use $a_j = a_{j,0}\left(T - T^{(0)}_{c,j}\right)$. Assuming, for example, that $A_2 \neq 0$, we insert the stationary solution of the minimization with respect to A_2 and obtain an effective free energy for A_1:

$$F(A_1) = -\frac{a_2^2}{4u_2} + \frac{a_1}{2}\left(1 - \frac{\gamma a_2}{a_1 u_2}\right)A_1^2 + \frac{u_1}{4}\left(1 - \frac{\gamma^2}{u_1 u_2}\right)A_1^4. \quad (11)$$

Assuming the opposite switches 1↔2. In both cases, the new quartic term becomes negative if $\gamma^2 > u_1u_2$, signalling a first-order transition. This corresponds to a bicritical point. If $\gamma^2 < u_1u_2$, the transition is of the second order and both transitions meet at a tetracritical point (Extended Data Fig. 2).

Consider now the transition temperature of phase 1 in the presence of order by phase 2. It holds that

$$T_{c,1} = T^{(0)}_{c,1} + \gamma\frac{a_{2,0}\left(T^{(0)}_{c,2} - T^{(0)}_{c,1}\right)}{\gamma a_{2,0} - u_2 a_{1,0}} \quad (12)$$

whereas in the opposite case (1↔2), we have

$$T_{c,2} = T_{c,2}^{(0)} + \gamma \frac{a_{1,0}\left(T_{c,1}^{(0)} - T_{c,2}^{(0)}\right)}{\gamma a_{1,0} - u_1 a_{2,0}} \tag{13}$$

For $\gamma < \sqrt{u_1 u_2}$, $T_{c,1} = T_{c,2}$ is only possible if $T_{c,1}^{(0)} = T_{c,2}^{(0)}$, which implies that $T_{c,j} = T_{c,j}^{(0)}$. This is where the two bare transitions meet.

Let us now consider the case in which the bare transition temperatures are controlled by pressure p such that

$$\begin{aligned} T_{c,1}^{(0)} &= T^* - \alpha_1 (p - P^*), \\ T_{c,2}^{(0)} &= T^* + \alpha_2 (p - P^*), \end{aligned} \tag{14}$$

where α_j are assumed positive. The tetracritical point is then at (T^*, P^*). Consider now the regime $T_{c,1} < T_{c,2}$. Then, it follows that

$$T_{c,1} = T^* - \alpha_1 (p - P^*)\left(1 - \gamma \frac{a_{2,0}\,(1 + \alpha_2/\alpha_1)}{\gamma a_{2,0} - u_2 a_{1,0}}\right) \tag{15}$$

When the slope of $T_{c,1}$ does not change substantially in the presence of phase 2, it must hold that

$$\frac{(1 + \alpha_2/\alpha_1)}{|1 - u_2 a_{1,0}/\gamma a_{2,0}|} \ll 1. \tag{16}$$

Suppose the two slopes α_1 and α_2 are of the same order of magnitude. It must hold that $u_2 a_{1,0}$ is much larger than $\gamma a_{2,0}$.

Consider now the opposite regime in which $T_{c,2} < T_{c,1}$. Then, it follows that

$$T_{c,2} = T^* + \alpha_2 (p - p^*)\left(1 - \gamma \frac{a_{1,0}\,(1 + \alpha_1/\alpha_1)}{\gamma a_{1,0} - u_1 a_{2,0}}\right) \tag{17}$$

The back bending of the phase line implies that $\frac{dT_{c,2}}{dp} < 0$ in the presence of the order of ψ_1. Hence, it must hold that

$$\gamma \frac{a_{1,0}\,(1 + \alpha_1/\alpha_1)}{\gamma a_{1,0} - u_1 a_{2,0}} > 1 \tag{18}$$

A necessary condition for this to happen is that

$$\gamma > \frac{a_{2,0}}{a_{1,0}} u_1 \tag{19}$$

The slope is particularly large if γ is only slightly larger than $\frac{a_{2,0}}{a_{1,0}} u_1$ and if $\gamma a_{1,0}$ is not too small.

To summarize, we have the following conditions:

$$\begin{aligned} &0 < \gamma < \sqrt{u_1 u_2} \\ &\gamma \ll \tfrac{a_{1,0}}{a_{2,0}} u_2 \\ &\gamma > \tfrac{a_{2,0}}{a_{1,0}} u_1, \end{aligned} \tag{20}$$

which follow from the existence of a tetracritical point, the weak change in slope of $T_{c,1}$ and the back bending of $T_{c,2}$, as discussed in the main text.

In our free energy expansion, we have a choice to properly normalize the order parameters. Hence, we can independently rescale the two order parameters as

$$\begin{pmatrix} \psi_1 \\ \psi_2 \end{pmatrix} \to \begin{pmatrix} s_1 \psi_1 \\ s_2 \psi_2 \end{pmatrix}. \tag{21}$$

This would not be allowed for a two-dimensional irrep, where the components transform into each other under certain symmetry operations and only $s_1 = s_2$ is allowed. We can use this freedom to transform the quadratic terms such that $(a_{1,0}, a_{2,0}) \to (s_1^2 a_{1,0}, s_2^2 a_{2,0})$. If one then chooses $s_2 = \sqrt{\frac{a_{1,0}}{a_{2,0}}} s_1$, it follows $a_{1,0} = a_{2,0}$. Then, we obtain the constraints given in the main text.

Heat capacity jumps. The extra heat capacity (relative to the normal state) in a phase with $\psi_1 \neq 0$ and $\psi_2 = 0$ is

$$\delta C_1 = \frac{a_{1,0}^2 T}{2u_1}, \tag{22}$$

whereas the opposite case ($\psi_1 = 0$ but $\psi_2 \neq 0$) yields

$$\delta C_2 = \frac{a_{2,0}^2 T}{2u_2}, \tag{23}$$

On the other hand, the heat capacity for the state in which both order parameters are finite is

$$\begin{aligned} \delta C_{12} &= \frac{a_{2,0}^2 u_1 + a_{2,0}^2 u_2 - 2a_{1,0}a_{2,0}\gamma}{2(u_1 u_2 - \gamma^2)} T \\ &= \frac{\left(a_{2,0}\sqrt{u_1} - a_{2,0}\sqrt{u_2}\right)^2 + 2a_{1,0}a_{2,0}(\sqrt{u_1 u_2} - \gamma)}{2(u_1 u_2 - \gamma^2)} T \end{aligned}. \tag{24}$$

The last line merely shows that $\delta C_{12} > 0$.

Hence, the jumps of the heat capacity at the upper, single transitions are

$$\frac{\Delta C(T_{c,1}^{(0)})}{T_{c,1}^{(0)}} = \frac{a_{1,0}^2}{2u_1} \text{ and } \frac{\Delta C(T_{c,2}^{(0)})}{T_{c,2}^{(0)}} = \frac{a_{2,0}^2}{2u_2}. \tag{25}$$

For the jump from a phase with ($\psi_1 = 0$ and $\psi_2 \neq 0$) to a phase with ($\psi_1 \neq 0$ and $\psi_2 \neq 0$) at $T_{c,1}$, we get

$$\frac{\Delta C(T_{c,1})}{T_{c,1}} = \frac{\delta C_{12}(T_{c,1}) - \delta C_2(T_{c,1})}{T_{c,1}} = \frac{(a_{1,0}u_2 - a_{2,0}\gamma)^2}{2u_2(u_1 u_2 - \gamma^2)}. \tag{26}$$

If we now analyse the ratio between the lower and upper transition, it follows that

$$\frac{T_{c,2}^{(0)} \Delta C(T_{c,1})}{T_{c,1} \Delta C(T_{c,2}^{(0)})} = \frac{\left(\frac{a_{1,0}}{a_{2,0}} u_2 - \gamma\right)^2}{u_1 u_2 - \gamma^2}. \tag{27}$$

We can also analyse the jump from a phase with ($\psi_1 \neq 0$ and $\psi_2 \neq 0$) to a phase with ($\psi_1 \neq 0$ but $\psi_2 = 0$) in the low-T phase (because of back bending) at $T_{c,2}$:

$$\frac{\Delta C(T_{c,2})}{T_{c,2}} = \frac{\delta C_1(T_{c,2}) - \delta C_{12}(T_{c,2})}{T_{c,2}} = -\frac{(a_{2,0}u_1 - a_{1,0}\gamma)^2}{2u_1(u_1 u_2 - \gamma^2)}, \tag{28}$$

that is, the heat capacity should have a negative jump as one enters SC1 through the back-bent phase transition.

Microscopic derivation of GL coefficients

Let us next get a microscopic understanding of the coefficients of the GL theory. To this end, we start from an effective Fermi liquid description in terms of well-defined quasiparticles, even if those excitations are the result of strong electronic interactions. Hence, we start from a Bogoliubov–de Gennes Hamiltonian:

$$\hat{H}_{\mathrm{BdG}} = \sum_{\mathbf{k}} \left(\mathbf{c}_{\mathbf{k}}^\dagger \xi(\mathbf{k}) \mathbf{c}_{\mathbf{k}} + \frac{1}{2} \mathbf{c}_{\mathbf{k}}^\dagger \Delta(\mathbf{k}) \mathbf{c}_{-\mathbf{k}}^{\dagger T} + \frac{1}{2} \mathbf{c}_{-\mathbf{k}}^T \Delta^\dagger(\mathbf{k}) \mathbf{c}_{\mathbf{k}} \right). \tag{29}$$

As we want to achieve a description in terms of a multiorbital problem with spin–orbit interactions, $\mathbf{c}_\mathbf{k}$ is a vector of the annihilation operator of electrons in bands with different pseudo-spins. If we consider a system with inversion symmetry and TRS in the normal state, each $\mathbf{k}$ state is doubly (Kramers) degenerate. Except for this Kramers degeneracy, the bands are for each $\mathbf{k}$ and in the generic case, non-degenerate in the vicinity of the Fermi surface. Hence, there is a single and unique band that belongs to a given Fermi momentum. This merely simplifies our notation and allows the use of momentum as the only relevant quantum number. Let us focus on the case in which both order parameters are peudo-spin triplets have the structure

$$\Delta(\mathbf{k}) = i\sigma_y\left(\psi_1\mathbf{\Delta}_1(\mathbf{k}) + \psi_2\mathbf{\Delta}_2(\mathbf{k})\right)\cdot\boldsymbol{\sigma}. \tag{30}$$

where σ are Pauli matrices, acting in the pseudo-spin space. The $\mathbf{\Delta}_{1,2}(\mathbf{k})$ are form factors of the pairing states that determine the spin and momentum structure of the Cooper pairs. For example, for a state that transforms under the B_{1u} irrep holds

$$\mathbf{\Delta}(\mathbf{k}) = \phi_x\mathbf{e}_x\sin k_y b + \phi_y\mathbf{e}_y\sin k_x a + \phi_z\mathbf{e}_z\sin\frac{k_x a}{2}\sin\frac{k_y b}{2}\sin\frac{k_z c}{2}, \tag{31}$$

where a, b and c are the unit-cell lattice constants in the corresponding directions. Other irreps can easily be described accordingly. These form factors of the pairing states require an appropriate normalization, which we discuss below. Integrating out the fermions and expanding the free energy of the system in terms of the two order parameters ψ_1 and ψ_2 then yields some microscopic expressions for the parameters of the GL expansion.

To express the coefficients of the energy expansions, it is useful to use the following notation:

$$\langle\mathbf{\Delta}_i|\mathbf{\Delta}_j|=\rangle\int\frac{dS}{|v(\mathbf{k})|}\mathbf{\Delta}_i^*(\mathbf{k})\cdot\mathbf{\Delta}_j(\mathbf{k}), \tag{32}$$

$$\langle\mathbf{\Delta}_i\otimes\mathbf{\Delta}_k|\mathbf{\Delta}_j\otimes\mathbf{\Delta}_m|=\rangle\int\frac{\mathrm{d}S}{|v(\mathbf{k})|}(\mathbf{\Delta}_i^*(\mathbf{k})\cdot\mathbf{\Delta}_j(\mathbf{k}))(\mathbf{\Delta}_k^*(\mathbf{k})\cdot\mathbf{\Delta}_l(\mathbf{k})), \tag{33}$$

where integration is performed over the Fermi surface and states are weighted by the inverse Fermi velocity. We then obtain for the corresponding coefficients in the GL expansion:

$$|\psi_1|^2 : a_{1,0} = \frac{\langle\mathbf{\Delta}_1|\mathbf{\Delta}_1|\rangle}{T_{\mathrm{c},1}^{(0)}}, \tag{34}$$

$$|\psi_2|^2 : a_{2,0} = \frac{\langle\mathbf{\Delta}_2|\mathbf{\Delta}_2|\rangle}{T_{\mathrm{c},2}^{(0)}}, \tag{35}$$

$$|\psi_1|^4 : u_1 = \frac{7\zeta(3)}{2\pi^2(T)^2}\left(2\langle\mathbf{\Delta}_1\otimes\mathbf{\Delta}_1|\mathbf{\Delta}_1\otimes\mathbf{\Delta}_1\rangle - \langle\mathbf{\Delta}_1\otimes\mathbf{\Delta}_1^*|\mathbf{\Delta}_1^*\otimes\mathbf{\Delta}_1\rangle\right), \tag{36}$$

$$|\psi_2|^4 : u_2 = \frac{7\zeta(3)}{2\pi^2(T)^2}\left(2\langle\mathbf{\Delta}_2\otimes\mathbf{\Delta}_2|\mathbf{\Delta}_2\otimes\mathbf{\Delta}_2\rangle - \langle\mathbf{\Delta}_2\otimes\mathbf{\Delta}_2^*|\mathbf{\Delta}_2^*\otimes\mathbf{\Delta}_2\rangle\right), \tag{37}$$

$$\begin{aligned}|\psi_1|^2|\psi_2|^2 : \gamma_1 = \frac{7\zeta(3)}{4\pi^2(T)^2}\,&(4\langle\mathbf{\Delta}_1\otimes\mathbf{\Delta}_2|\mathbf{\Delta}_1\otimes\mathbf{\Delta}_2\rangle\\ &+4\langle\mathbf{\Delta}_2\otimes\mathbf{\Delta}_2^*|\mathbf{\Delta}_1\otimes\mathbf{\Delta}_1^*\rangle - 4\langle\mathbf{\Delta}_1^*\otimes\mathbf{\Delta}_1|\mathbf{\Delta}_2\otimes\mathbf{\Delta}_2^*\rangle),\end{aligned} \tag{38}$$

$$\psi_1^2\psi_2^{*2} : \gamma_2 = \frac{7\zeta(3)}{4\pi^2(T)^2}\left(2\langle\mathbf{\Delta}_2\otimes\mathbf{\Delta}_2|\mathbf{\Delta}_1\otimes\mathbf{\Delta}_1\rangle - \langle\mathbf{\Delta}_1^*\otimes\mathbf{\Delta}_2|\mathbf{\Delta}_1\otimes\mathbf{\Delta}_2^*\rangle\right), \tag{39}$$

$$\gamma = \gamma_1 - |\gamma_2|. \tag{40}$$

These results allow for several rather general insights:

- The above freedom to rescale the order parameters is equivalent to choosing an appropriate normalization of $\mathbf{\Delta}_{1,2}(\mathbf{k})$. For example, if we adopt the natural normalization

$$\langle\mathbf{\Delta}_i|\mathbf{\Delta}_j|=\rangle\int\frac{dS}{|v|}\mathbf{\Delta}_i^\dagger\cdot\mathbf{\Delta}_j = \delta_{ij}, \tag{41}$$

- we obtain $a_{i,0} = 1/T_{\mathrm{c},i}^{(0)}$. Close to the tetracritical point, where the two transitions merge, this is essentially equivalent to setting $a_{1,0} = a_{2,0}$.
- If we now ask how the hierarchy $u_1 < \gamma \ll u_2$, which follows from the phase diagram, can be realized, it is not straightforward to identify the two form factors $\mathbf{\Delta}_1(\mathbf{k})$ and $\mathbf{\Delta}_2(\mathbf{k})$ for the pairing states SC1 and SC2 that share the same normalization of $\mathbf{\Delta}_i^*(\mathbf{k})\cdot\mathbf{\Delta}_i(\mathbf{k})$ (equation (41)), yet whose square differs sufficiently to ensure $u_1 \ll u_2$. For pairing states such as that in equation (31), whose leading harmonics vary smoothly throughout the Brillouin zone, achieving this separation is difficult for Fermi surface sheets that contribute similarly to the density of states. However, in our normalization scheme, states are weighted by their inverse Fermi velocity, that is, their contribution to the density of states. If the orbital weight of $\mathbf{\Delta}_{1,2}(\mathbf{k})$ differs substantially between bands with large and small Fermi velocities, this issue may be resolved and the observed phase diagram can be explained. We, therefore, conclude that it is rather likely that the superconducting states SC1 and SC2 differ substantially in their orbital composition on the heavy U5*f* bands, compared with bands with U6*d* or Te5*p* character. In particular, the larger value of u_2 implies a smaller contribution of U5*f* orbitals in SC2.
- The sign of the expansion coefficient γ_2 determines whether TRS is broken in the SC1+SC2 phase. If we consider so-called unitary superconducting states, the $\mathbf{\Delta}_{1,2}$ are real and we obtain

$$\gamma_2 = \frac{7\zeta(3)}{4\pi^2(T)^2}\int\frac{\mathrm{d}S}{|v(\mathbf{k})|}|\mathbf{\Delta}_1|^2|\mathbf{\Delta}_2|^2(\cos 2\theta_\mathbf{k}), \tag{42}$$

- where $\theta_\mathbf{k}$ is the angle between $\mathbf{\Delta}_1(\mathbf{k})$ and $\mathbf{\Delta}_2(\mathbf{k})$. Thus, whenever the spin structure of the two triplet states is such that, on averaging over all Fermi surface sheets, one predominantly has $\theta_\mathbf{k} \approx 0$ or $\theta_\mathbf{k} \approx \pi$. That is, when the spin structures of the two states are aligned in momentum space, it follows that $\gamma_2 > 0$ and TRS is broken; otherwise, TRS remains preserved. Given our above insights for the orbital composition of the pairing states, it seems natural that this spin alignment of the pairing states only has to take place on the Fermi surface sheets dominated by U5f states, since this Fermi surface sheet dominates the total sum over all states.

General thermodynamic constraints

In this section, we show that the phase diagram observed in this work (Fig. 2a) is consistent with the constraints imposed by the measured specific heat. Following a similar analysis performed in UPt_3 (ref. 11), and using their notation, the normal state, SC2, SC1 and SC1+SC2 phases are referred to as N, A, B and C, respectively. The slopes dP/dT of the AN, BN, CA and CB phase boundaries are defined as p_1, p_2, p_3 and p_4, respectively (Extended Data Fig. 3). The difference in specific heat (denoted by α in ref. 11) across any phase boundary IJ is $\Delta\alpha_{IJ} \equiv \alpha_I - \alpha_J$. We also define ratios of the specific heat jumps as follows:

$$r_3 = \left(\frac{\Delta\alpha_{CA}}{\Delta\alpha_{BN}}\right)^{1/2}, \qquad r_1 = \left(\frac{\Delta\alpha_{AN}}{\Delta\alpha_{BN}}\right)^{1/2}.$$

Since the line CB is a second-order phase boundary, Ehrenfest's relations require that[11]

$$1 - \frac{p_2}{p_3} = \left(\frac{p_2}{p_1} - 1\right)r_1\frac{r_1 r_3 \pm (r_1^2 + r_3^2 - 1)^{1/2}}{(1 - r_1^2)r_3}. \tag{43}$$

The positivity of the term in the square root gives us our first constraint. Since $\Delta\alpha_{CB} = \Delta\alpha_{BN}(r_1^2 + r_3^2 - 1)$, this requires $\Delta\alpha_{CB} > 0$, that is, when the temperature is lowered across the CB phase boundary, the heat capacity jumps down; alternatively, the elastic constant jumps up. This is exactly what we observe. It is interesting to note that in ref. 11, $\Delta\alpha_{CB} > 0$ is used to conclude that C must be a lower-temperature phase than B, presumably owing to a lack of observed downward jumps in heat capacity at the time. We experimentally observe an upward jump in the elastic constant in this work, requiring a downward jump in the specific heat capacity to be consistent with Ehrenfest relations, thereby requiring B (that is, SC1) to be the lower-temperature phase. Later in this section, we show that this still allows all constraints to be satisfied.

Defining

$$r_4 \equiv \left(\frac{\Delta\alpha_{CB}}{\Delta\alpha_{BN}}\right)^{1/2} = (r_1^2 + r_3^2 - 1)^{1/2}, \tag{44}$$

the continuity of the free energy across the CB phase boundary imposes the second constraint[11]:

$$\frac{1 - p_2/p_4}{1 - p_2/p_1} = \frac{\mp(r_1/r_4)r_3 - r_1^2}{1 - r_1^2}. \tag{45}$$

From the phase boundaries measured in this work, we have the slopes $p_1 = 2.9\ \mathrm{K\ GPa^{-1}}$, $p_2 = p_3 = -1.08\ \mathrm{K\ GPa^{-1}}$ and $p_4 = -77.9\ \mathrm{K\ GPa^{-1}}$. Using these, for the left-hand side, we get $\frac{1-p_2/p_4}{1-p_2/p_1} = 0.71$. We use the quantitative specific heat values from refs. 24,25 to obtain $r_3 = 0.984$ and $r_1 = 0.027$, which gives us

$$\frac{r_1^2}{r_4^2} = \frac{\alpha_{AN}}{\alpha_{CB}} = 0.52 \tag{46}$$

That is, the specific heat jump across the CB (T_{c2}^*) phase boundary must be approximately twice the specific heat jump across the AN (T_{c2}) phase boundary. Although we do not measure the specific heat jump at T_{c2}^*, the GL theory we construct gives us $\alpha_{CB} \ll \alpha_{BN}$ and $\alpha_{AN} \ll \alpha_{BN}$, consistent with this constraint.

Using $r_4 = (r_1^2 + r_3^2 - 1)^{1/2}$ in equation (43) gives us the final constraint:

$$\frac{1 - p_1/p_3}{1 - p_1/p_2} = \frac{r_3 \pm r_1 r_4}{(1 - r_1^2)r_3}. \tag{47}$$

Since we measure $p_2 = p_3$ in this work, the left-hand side of this constraint becomes $\frac{1-p_1/p_3}{1-p_1/p_2} = 1$. From the values of r_1, r_3 and equation (46), this gives us for the right-hand side as $\frac{r_3 \pm r_1 r_4}{(1-r_1^2)r_3} = 0.9997$, satisfying the final constraint.

Symmetry analysis

The application of a b-axis magnetic field reduces the point group symmetry of UTe_2 from D_{2h} to C_{2h}, removing the two mirror planes containing the magnetic field vector.

The fact that we still see second-order phase transitions between the SC1 and SC2 superconducting states in Fig. 1 allows us to constrain the possible symmetries of the SC1+SC2 order in UTe_2. In particular, SC1 and SC2 must belong to separate irreducible representations of the reduced C_{2h} symmetry to allow for a second-order phase transition between them. In Extended Data Table 1, we show the mapping of each D_{2h} irrep when a symmetry-breaking b-axis field is applied. We can then rule out the $A_u + B_{2u}$ and $B_{1u} + B_{3u}$ combinations (written in the D_{2h} nomenclature) among the odd-parity irreps, since both components map onto the same irrep in C_{2h}, and therefore, any transition between these two states would generically be of the first order.

Additionally, the lack of a jump in c_{55} at $P > P\star$ also constrains certain combinations. Since c_{55} measures the coupling of the ϵ_{xz} strain to the order parameter, order parameter combinations that couple linearly to ϵ_{xz} may also be ruled out[5,12]. This also rules out the $A_u + B_{2u}$ and $B_{1u} + B_{3u}$ combinations among odd-parity representations.

Zero-pressure phase diagram

Although we do not apply magnetic fields large enough to reach the multicomponent state at ambient pressure, the B_b–P–T phase diagram (Fig. 4) allows us to constrain the $P = 0$ phase diagram as a function of temperature and b-axis magnetic field (Extended Data Fig. 4). The multicomponent state is accessible well within the reach of many commercially available superconducting magnets at fields over 12 T, enabling studies with more conventional techniques without the need of a pressure cell.

Data used for zero-field phase diagram construction

The full set of data we measure to construct the pressure–temperature phase diagram at zero field (Fig. 2) is shown in Extended Data Fig. 5. Superconducting transitions manifest as jumps in the compressional elastic constants c_{11} and c_{33}, and as kinks in the shear elastic constant c_{55}.

The c_{33} data shown here (Extended Data Fig. 5b) follow the same trend as c_{11} shown in the main text. We see a single transition as a downward jump at T_{c1} when $P < P\star$. For $P > P\star$, the T_{c2} transition appears as a large downward jump, whereas the T_{c1} transition is too small to be seen on the scale shown in Extended Data Fig. 5b (Extended Data Fig. 6a,b shows the c_{33} data at 0.36 and 0.77 GPa on a larger scale, with insets clearly showing the downward jumps at T_{c1}). At $P = 0.21$ GPa, we see an upward jump at T_{c2}^*. Note that there is a subtle kink about 50 mK below T_{c2}^*, which we attribute to pressure inhomogeneity within the sample. We attribute this to either small internal inhomogeneities or small external pressure inhomogeneities in the sample: because T_{c2}^* drops by nearly 1.5 K over a 0.01-GPa pressure range, even parts-per-thousand inhomogeneities in the pressure can lead to smearing of T_{c2}^* over tens of millikelvins.

The c_{55} data are shown in Extended Data Fig. 5c, and exhibit kinks at the T_{c1} and T_{c2} superconducting transitions.

Absence of hysteresis at T_{c2}^*

To demonstrate that the T_{c2}^* transition measured in this work is of the second order, we measure c_{33} and α_{33} whereas sweeping temperature up and down through T_{c2}^*. These data are shown in Extended Data Fig. 6c,d. Note the absence of any hysteresis.

Data used for B–T phase diagram construction

The full dataset used to construct the field–temperature phase diagrams in Fig. 3 is shown in Extended Data Figs. 7 and 8. Temperature sweeps of c_{33} and c_{55} near the tetracritical point are presented in Extended Data Fig. 7, whereas Extended Data Fig. 8 shows the corresponding field sweeps of c_{33} and α_{33} at the same pressures.

Constraining the T_{c2}^* phase boundary in B–P–T space

We obtain the T_{c2}^* phase boundary shown in Fig. 2 by constraining a sheet of T_{c2}^* phase transitions in B–P–T space and then projecting it onto $B_b = 0$. This is a stronger constraint than using the transitions we observe at $B_b = 0$ alone. We show this phase boundary along with all the T_{c2}^* transitions observed in this work in Extended Data Fig. 9.

Data availability

The data measured in this work are freely available via GitHub at https://github.com/CHiLL-Ramshaw/manuscripts-supporting_data/tree/main/2026_UTe2_Tetracriticality.

References

24. Vasina, T. et al. Quantitative thermodynamic study of superconducting and normal states in UTe_2 under pressure. *Phys. Rev. B* **113**, 235159 (2026).

25. Sakai, H. et al. Field induced multiple superconducting phases in UTe2 along hard magnetic axis. *Phys. Rev. Lett.* **130**, 196002 (2023).

Author contributions

B.J.R. and S.K. conceived the experiment. S.S. and J.P. grew and characterized the samples of UTe_2. S.K. and J.D. prepared the samples for ultrasound measurements and collected the data. S.K. analysed the data and produced the figures. J.S. and A.D.K. performed the theoretical calculations. B.J.R. and S.K. wrote the manuscript, with input from all authors. B.J.R. supervised the project.

Funding

Research at Cornell was supported by the Department of Energy, Office of Basic Energy Sciences, via award number DE-SC-0026003 (ultrasound measurements and data analysis). Research at the University of Maryland was supported by the Gordon and Betty Moore Foundation's EPiQS Initiative via grant number GBMF9071 (materials synthesis), the Department of Energy, Office of Basic Energy Sciences, via award number DE-SC-0019154 (sample characterization), the NIST Center for Neutron Research, and the Maryland Quantum Materials Center. Theory work was supported by German Research Foundation TRR 288-422213477 ELASTO-Q-MAT, A07 (A.D.K. and J.S.) and grant SFI-MPS- NFS-00006741-05 from the Simons Foundation (J.S.).

Competing interests

The authors declare no competing interests.

Additional information

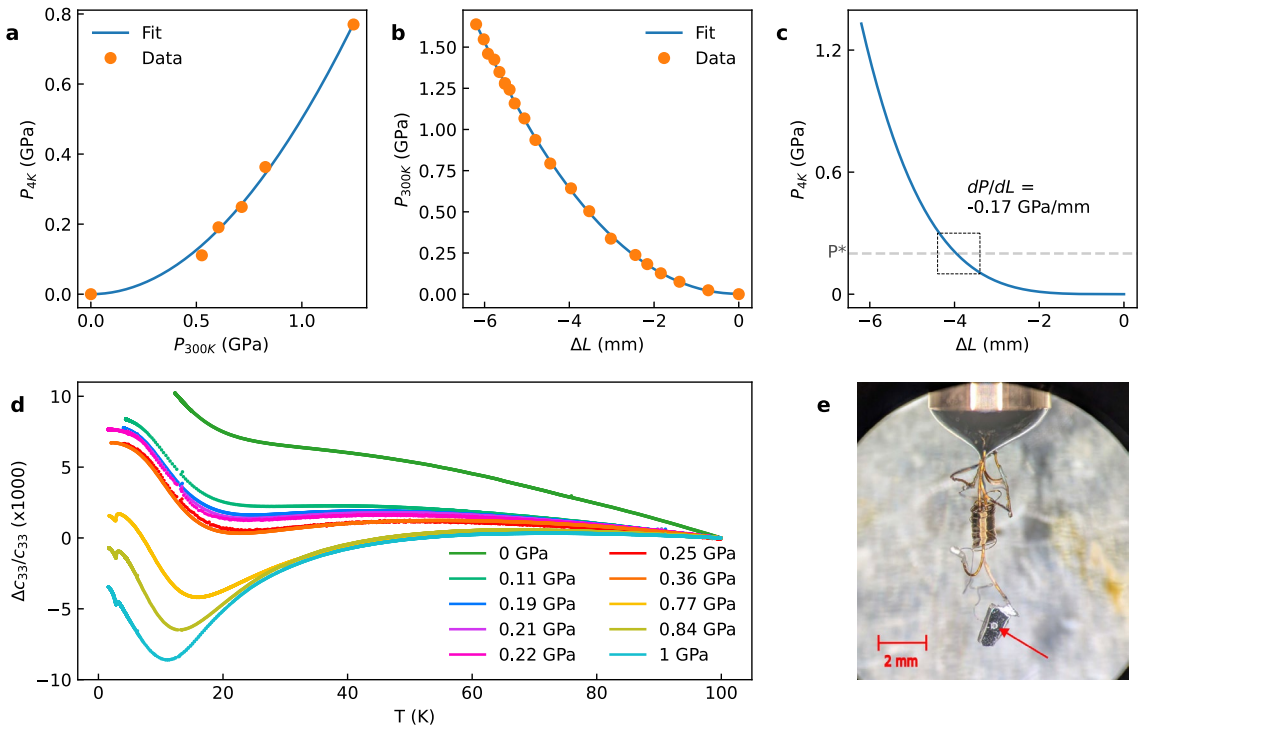
Extended data is available for this paper at https://doi.org/10.1038/s41567-026-03504-z.

Correspondence and requests for materials should be addressed to B. J. Ramshaw.

Peer review information *Nature Physics* thanks Friedrich Grosche, Yoichi Yanase and the other, anonymous, reviewer(s) for their contribution to the peer review of this work.

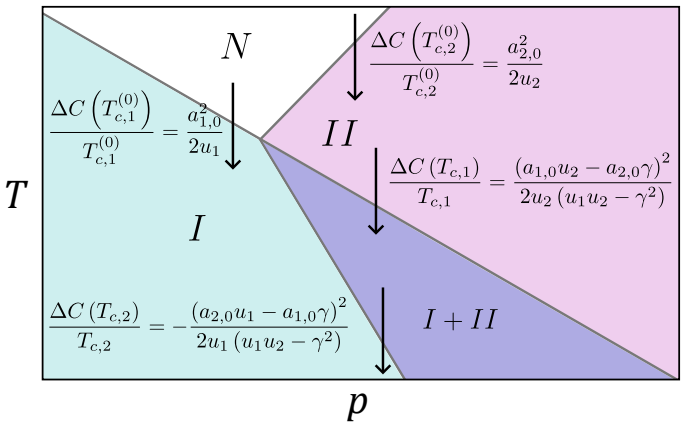
Reprints and permissions information is available at www.nature.com/reprints.

https://doi.org/10.1038/s41567-026-03504-z



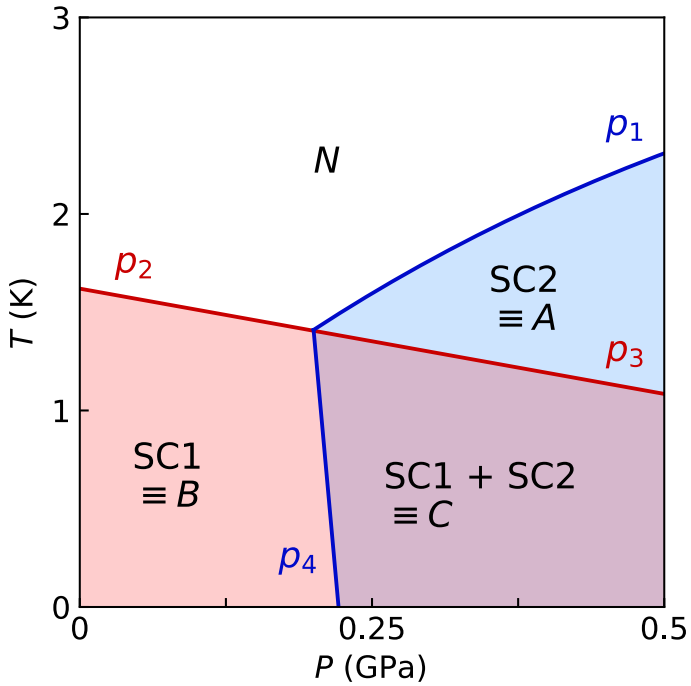
Extended Data Fig. 1 | Accurately tuning the pressure at low temperature. **a**) The pressure of the sample at low temperature (4 K) as measured by T_{c1} and T_{c1} versus the pressure as measured by a manganin manometer at room temperature. We fit the data to a second order polynomial. **b**) The pressure measured at room temperature versus the change in length of the pressure cell, proportional to the change in volume of the pressure medium. We fit the data to a fourth order polynomial. **c**) Combining the fits in (**a**) and (**b**), the predicted low-temperature pressure versus the pressure cell length. The slope of this curve in the region close to the tetracritical point (dashed box) is used to accurately change the pressure of the sample by changing the length of the pressure cell. **d**) c_{33} data up to 100 K, used as a consistency check as we tune pressure. The minimum in the data occurs due to the Kondo effect and is highly sensitive to pressure. **e**) Sample when mounted inside the pressure cell. Seen are the coil of manganin wire used as a manometer at room temperature, along with the sample of UTe2. The pulse-echo transducer is indicated by a red arrow and is seen as a small silver dot on the sample. Because of its small size (~100μm), we measure a small sample volume – given by the area of the transducer (~ π(100μm)^2) times the thickness of the sample (~300 μm). This is much smaller than in other techniques, leading to a much lower pressure inhomogeneity.

https://doi.org/10.1038/s41567-026-03504-z



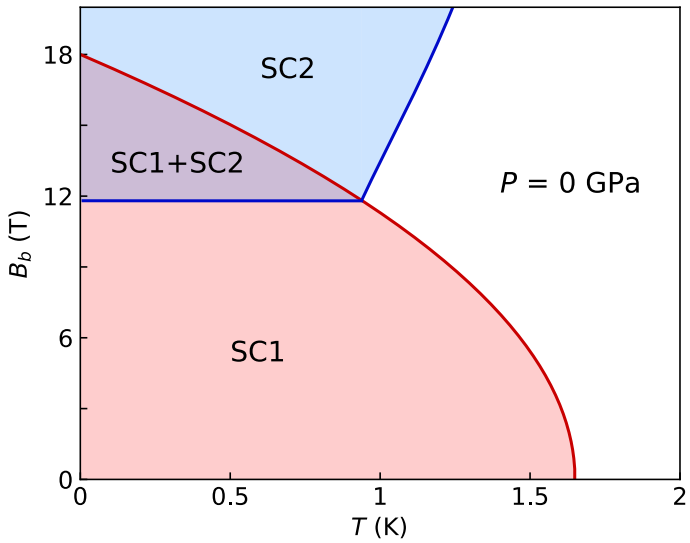
Extended Data Fig. 2 | Phase Diagram and Heat Capacity Jumps. The temperature and pressure axes are denoted by *T* and *p* respectively. The SC1, SC2 and SC1+SC2 states are denoted by I, II and I+II respectively. Jumps in $\Delta C/T$ occur at each phase boundary, with arrows indicating the crossing direction.

https://doi.org/10.1038/s41567-026-03504-z



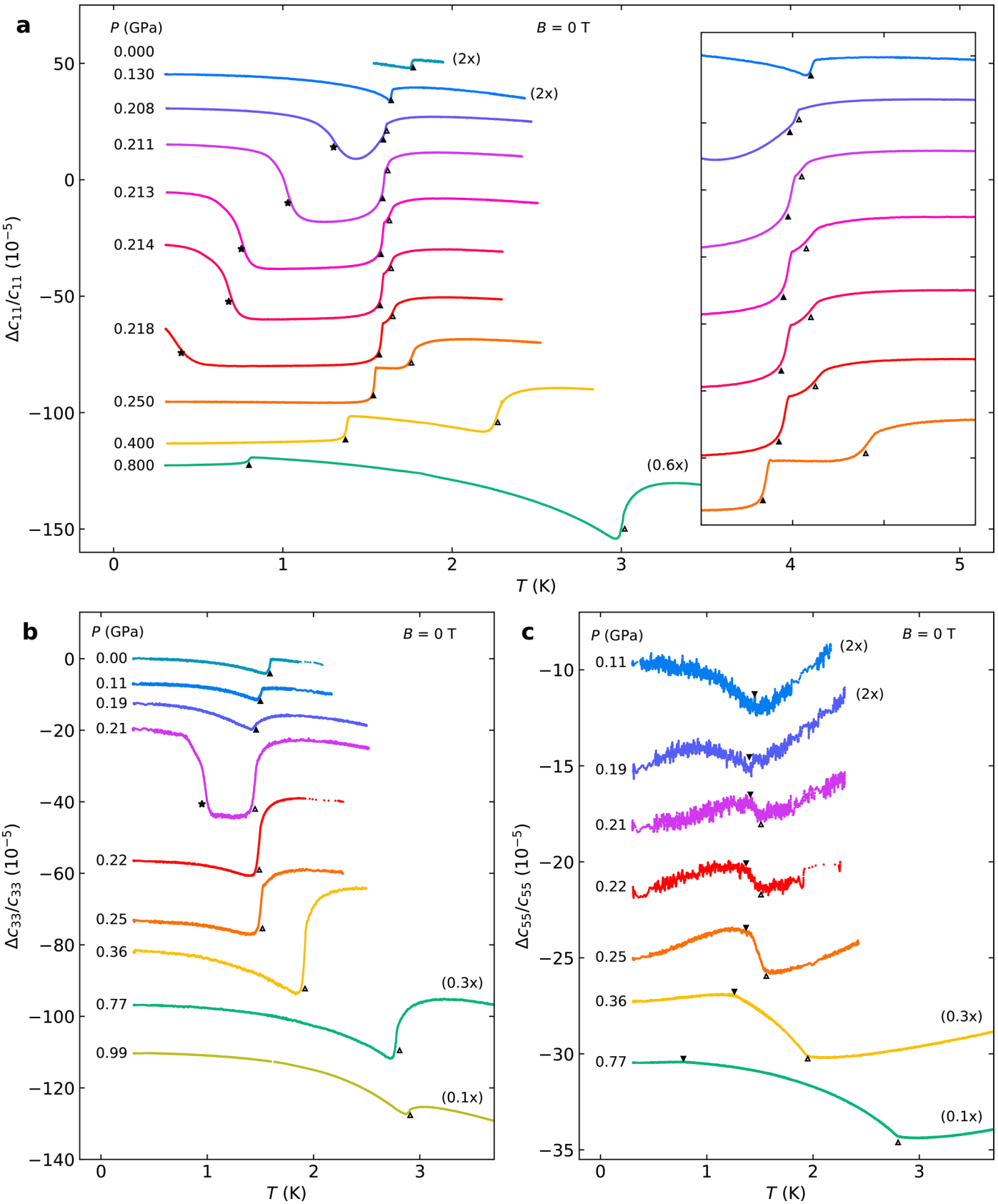
Extended Data Fig. 3 | The P-T phase diagram with definitions used in General Thermodynamic Constraints. The normal state, SC2, SC2 and SC1+SC2 phases are referred to as N, A, B and C respectively, following the notation used in ref. 7. The slopes of the AN, BN, CA and CB phase boundaries are defined to be p_1, p_2, p_3 and p_4 respectively.

https://doi.org/10.1038/s41567-026-03504-z



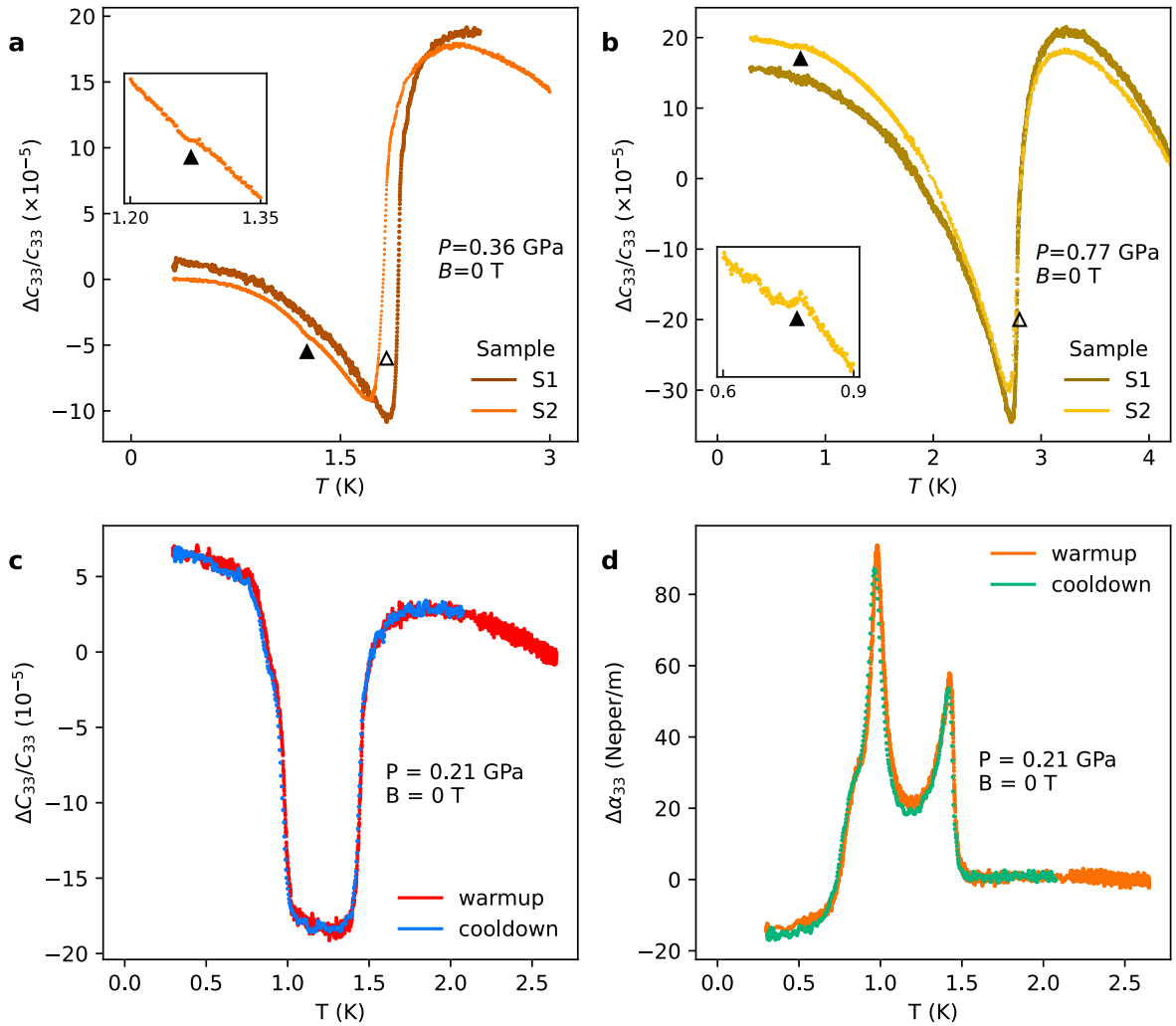
Extended Data Fig. 4 | Ambient pressure phase diagram. The $B_b - P - T$ phase diagram we construct in Fig. 4 of the main text constrains the zero-pressure phase boundaries as a function of magnetic field and temperature. SC1 and SC2 phases are shaded red and blue respectively. The SC1+SC2 multi-component state, shaded purple, is accessible between 12 and 18 T at ambient pressure. The T_{c1} and T_{c2} phase boundaries we observe agree quantitatively with previous measurements of the phase diagram[23,25].

https://doi.org/10.1038/s41567-026-03504-z



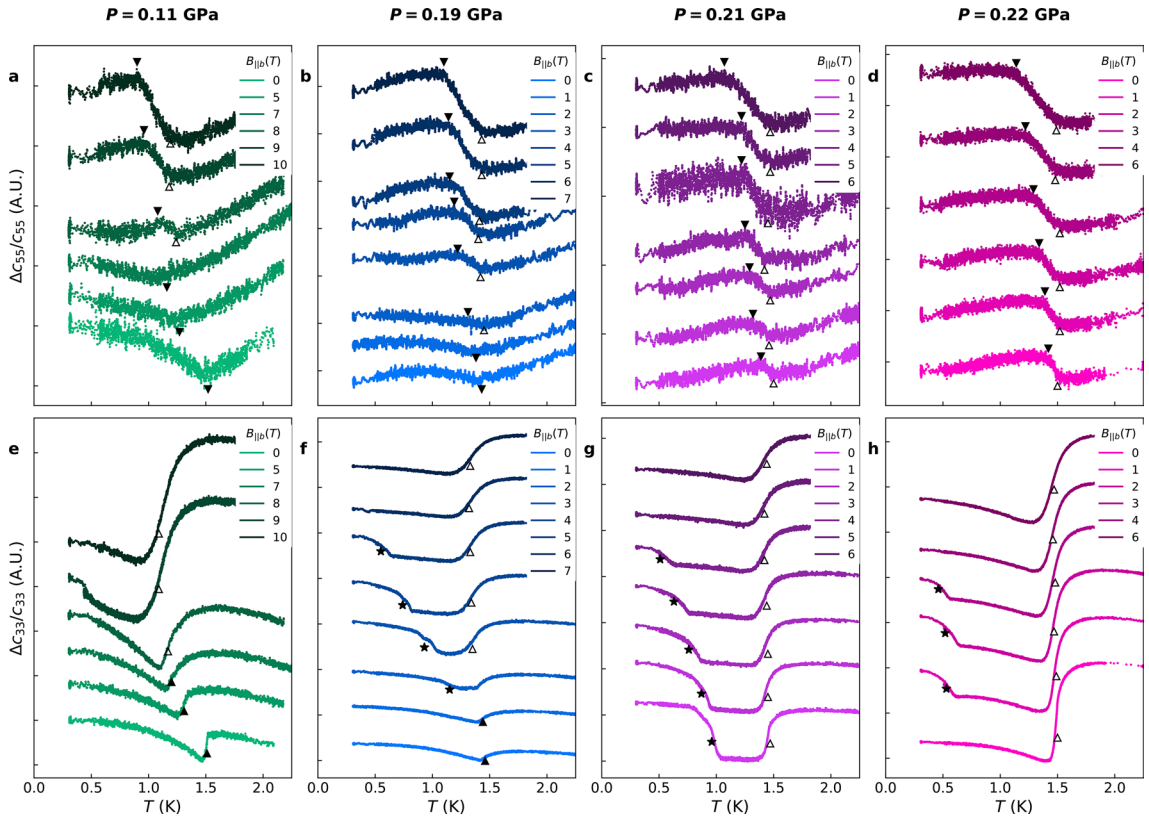
Extended Data Fig. 5 | Full set of c_{11}, c_{33} and c_{55} data used to construct the zero-field P-T phase diagram. (**a**) c_{11} data. The inset shows zoomed in c_{11} at pressures near P^*. (**b**) c_{33} data (**c**) c_{55} data, measured simultaneously with the c_{33} data. T_{c1}, T_{c2} and T^*_{c2} are marked by solid triangles, hollow triangles and stars respectively.

https://doi.org/10.1038/s41567-026-03504-z



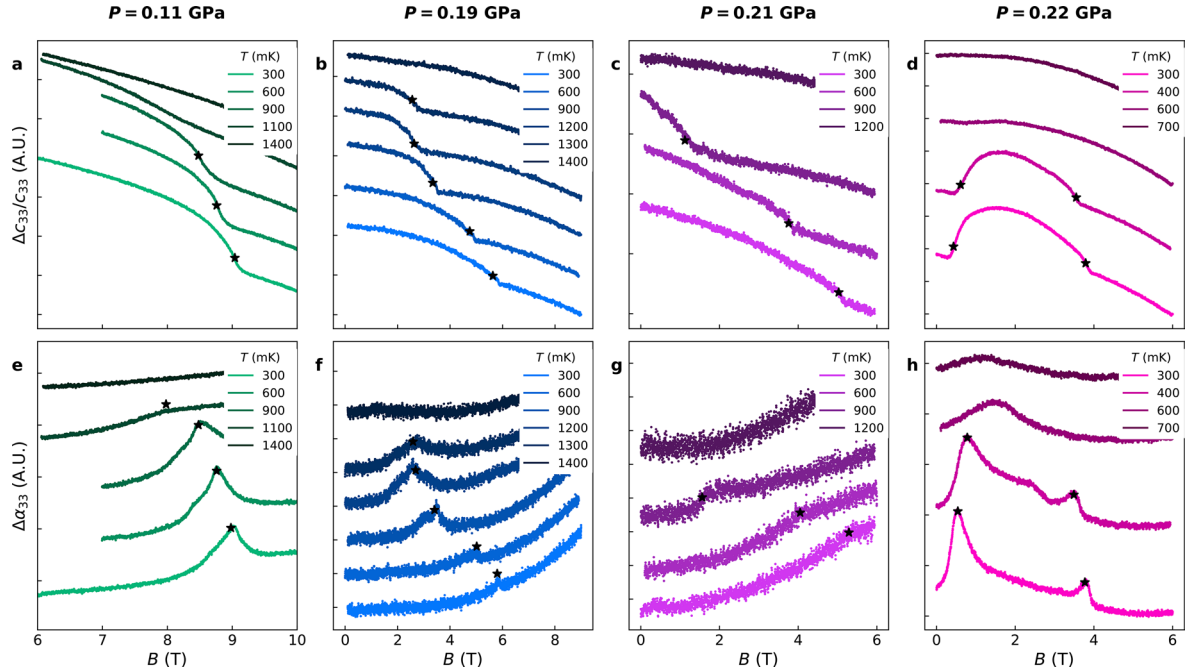
Extended Data Fig. 6 | Jumps in c_{33} at T_{c1}, and c_{33} and α_{33} when warming and cooling. (a) and (b) Although not visible on the scale of Extended Data Figure 5, we observe small downward jumps as the sample enters the SC1 state at T_{c1} for pressures $P > P^*$, marked by filled triangles. Note that these jumps are measured on a different sample S1 optimized for c_{33} measurement – c_{33} data at 0.36 and 0.77 GPa in Extended Data Figure 5 is sample S2. Insets: Data zoomed in on the transition at T_{c1}. (**c**) and (**d**) Absence of hysteresis at T^*_{c2}. c_{33} (**c**) and α_{33} (**d**) as a function of temperature, measured on cooling and warming the sample through T^*_{c2}. The absence of any hysteresis confirms that on cooling and warming the sample through T^*_{c2} is a second order phase transition.

https://doi.org/10.1038/s41567-026-03504-z



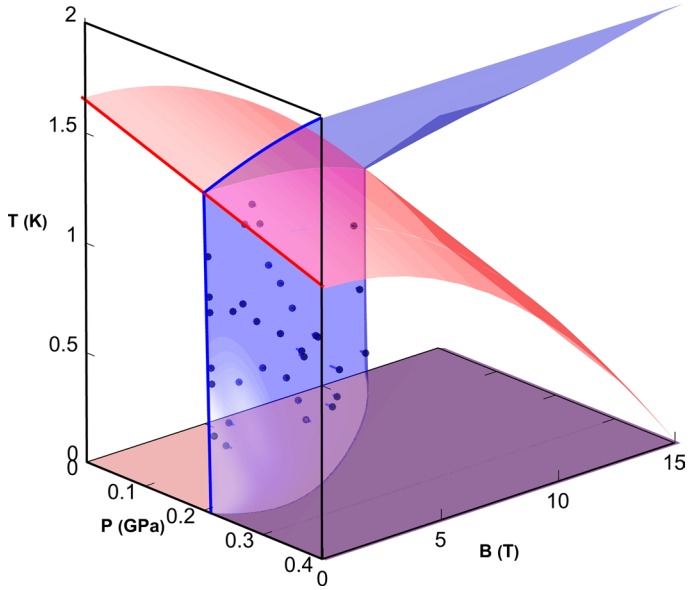
Extended Data Fig. 7 | Full set of c_{33} and c_{55} data measured as a function of temperature. (**a**-**d**) c_{55} at different pressures and magnetic fields, with kinks corresponding to the T_{c1} and T_{c2} transitions marked by solid and hollow triangles respectively. **e**-**h**) c_{33} at different pressures and magnetic fields. T_{c1}, T_{c2} and T^*_{c2} are marked by solid triangles, hollow triangles and stars respectively.

https://doi.org/10.1038/s41567-026-03504-z



Extended Data Fig. 8 | Full set of c_{55} and α_{33} data measured as a function of b-axis magnetic field. a-d) c_{33} at different temperatures and pressures. We observe a broad downward jump as the sample enters the SC2 state, marked by a solid black star. **e-h**) α_{33} data at different temperatures and pressures. We see an order parameter relaxation peak at the SC2 phase boundaries, marked by a solid black star.

https://doi.org/10.1038/s41567-026-03504-z



Extended Data Fig. 9 | The T^*_{c2} phase boundary constructed in this work. All the T^*_{c2} transitions we measure in this work are shown as solid black points, connected to the T^*_{c2} phase boundary (shown as a blue sheet) by thin blue lines. We obtain the zero-field phase boundary via the intersection of this sheet with the $B_b = 0$ plane (shown as a black frame).

https://doi.org/10.1038/s41567-026-03504-z

Extended Data Table 1 | A mapping between D_{2h} and C_{2h} irreps. in UTe_2

D_{2h} irrep.	C_{2h} irrep.
A_g	A_g
B_{1g}	B_g
B_{2g}	A_g
B_{3g}	B_g
A_u	A_u
B_{1u}	B_u
B_{2u}	A_u
B_{3u}	B_u